

# How rheological properties affect fine-line screen printing of pastes: a combined rheological and high-speed video imaging study

Chenhui Xu, Norbert Willenbacher

© American Coatings Association 2018

**Abstract** Fine-line screen printing is still a great challenge due to the lack of overall understanding between the rheological properties and screen printing process. Here, we prepared ZnO pastes including ethyl cellulose or Thixatrol Max as an additive introducing different physical mechanisms of structure and flow control. Yield stress, viscosity, and its recovery after high shear were obtained using rotational rheometry. Filament breakup was determined in uniaxial elongational tests. Pastes were printed using a commercial screen designed for Si-solar cell front-side metallization, and the process was monitored with high temporal and spatial resolution using a transparent glass substrate and a high-speed imaging setup. Length of the pre-injection zone ahead of the squeegee scales inversely with yield stress and length of the cling zone behind the squeegee is proportional to filament rupture strain, irrespective of used additive. Paste spreading observable at the busbar and fine-line intersection takes place within 100 ms, irrespective of sample composition, demonstrating that fine-line electrode width is determined within the pre-injection zone where the paste is under pressure. A simple flow model is proposed relating electrode width to the reciprocal product of yield stress and high shear viscosity consistent with experimental data including both types of pastes.

**Keywords** Fine-line screen printing, High-speed imaging, Rheology

**Electronic supplementary material** The online version of this article (<https://doi.org/10.1007/s11998-018-0091-2>) contains supplementary material, which is available to authorized users.

C. Xu (✉), N. Willenbacher  
Group Applied Mechanics (AME), Institute for Mechanical Process Engineering and Mechanics, Karlsruhe Institute of Technology, 76131 Karlsruhe, Germany  
e-mail: [chenhui.xu@student.kit.edu](mailto:chenhui.xu@student.kit.edu)

## Introduction

Due to its low cost and high throughput, screen printing is an essential step for electrode fabrication in many electronic devices, e.g., printed circuit boards,<sup>1,2</sup> thin-film transistors,<sup>3</sup> touch panel pattern,<sup>4</sup> low temperature co-fired ceramic devices,<sup>5,6</sup> or photovoltaic cells.<sup>7,8</sup> Considering cost and electronic performance, different kinds of conductive materials are formulated for screen-printable paste, including carbon,<sup>9,10</sup> copper,<sup>3,4</sup> or silver.<sup>11</sup>

Besides active solid particles, such pastes include organic solvents and additives providing stability during storage and appropriate flow behavior during the printing process. These ingredients may also affect the mechanical as well as electronic properties of the final printed electrodes. Different particle materials and surface treatments need different solvents and dispersants to get a well-dispersed and stable system. Binders are important to prove cohesion within the layer and the adhesion to the substrate after drying. In some applications, e.g., medical sensing, body motion detection, electronic skin, and healthcare monitoring, electrode flexibility is important to produce soft, deformable, and wearable devices.

The miniaturization of the electronic devices demands finer printed patterns for higher device density, e.g., modern smartphones chase higher screen-to-body ratio,<sup>12</sup> requiring narrower printed electrodes on the touch screen edge. Narrower printed electrodes reduce the shaded area on front-side of silicon solar cells, resulting in higher efficiency.<sup>13</sup> An improved conductor resolution in low temperature co-fired ceramic devices is mandatory for high-frequency applications, requiring a better control of electrode geometry.

Generally, screen-printable pastes are shear thinning, with low viscosity under high shear when pressed through the screen opening and high viscosity at rest to guarantee stability during storage and avoid spreading

after printing.<sup>14–17</sup> Such pastes often exhibit a so-called apparent yield stress, i.e., a minimum stress required to facilitate irreversible shear flow. Hoornstra et al. designed a rheological test to simulate the screen printing process, in which the pastes are treated with low, high, and low shear rates in sequence.<sup>17</sup> They postulated that fast recovery of viscosity after high shear restrains spreading. Wall slip can have a strong impact on paste deposit and electrode geometry and hence electrical performance of the printed devices.<sup>18,19</sup> Xu et al.<sup>19</sup> demonstrated that the paste deposit and electrode height increased whereas the area of the busbar/finger connection decreased with higher slip velocity during front-side metallization of solar cells. They employed a model system allowing for a wide range of wetting properties and slip velocity varying the mixing ratio of two organic co-solvents.

Riemer presented an analytical model, correlating the hydrostatic pressure on the squeegee and screen surface with printing parameters, i.e., printing speed  $V_{\text{print}}$ , squeegee angle  $\alpha$ , assuming the ink as a Newtonian fluid with viscosity  $\eta$ .<sup>20</sup> He calculated the pressure distribution within the paste roll ahead of the squeegee on the screen surface  $p_{\text{screen}} = f(\alpha) \cdot \eta \cdot V_{\text{print}} \cdot (1/r)$ , where the  $r$  is the distance from contact point between squeegee and screen. Considering the non-Newtonian characteristics, Glinski et al. simulated  $p_{\text{screen}}$  for stencil printing with CFD and assumed the viscosity of the solder paste  $\eta$  can be described with a so-called Cross model, taking into account a power-law-type shear thinning behavior as well as limiting viscosity values  $\eta_0$  and  $\eta_\infty$  at low and high shear rates, respectively.<sup>21</sup> Clements et al. did similar calculations assuming a power-law between shear stress and shear rate for the paste.<sup>22</sup> However, the screen-printable pastes, especially those for fine-line metallization, are Bingham pseudo-plastic fluids, with an additional yield stress  $\sigma_y$ , which has not been considered so far. Besides calculating  $p_{\text{screen}}$ , Riemer also introduced the definition of a cling zone, in which the screen remains in contact with the substrate due to paste stickiness.<sup>20</sup> Kapur et al. presented a mathematical model and simulated snap-off process in which the mesh separated from the substrate after paste filament extension, forming the mesh mark in the final printed film.<sup>23</sup>

Commercial, mass production of printed devices aims at ever higher printing speed  $V_{\text{print}}$  to achieve higher throughput, e.g., in solar cell front-side electrode metallization  $V_{\text{print}}$  typically reaches  $\sim 300$  mm/s.<sup>24</sup> It is difficult to investigate this process focusing on the micrometer length scale at such high speed. Moreover, opaque substrates, e.g., silicon wafers and ceramics, make it impossible to investigate the screen printing process from the bottom side. Therefore, there is still a lack of direct experimental investigations of the fine-line screen printing process. In this work, we have replaced the typical commercial substrate with a transparent glass plate, making it possible to record the process from the bottom side using a high-speed camera mounted onto a commercial screen printer.

With high enough frame rate (1000 fps) and suitable optics, it is possible to record the motion of the squeegee and screen as well as paste flow with 1 ms temporal and 0.75- $\mu\text{m}$  spatial resolution. Six zinc oxide (ZnO)-based model pastes were prepared with two different types of rheological additives, i.e., polymer binder and thixotropic agent, providing distinctly different flow characteristics. Varying additive concentration allowed for adjusting paste flow properties in a wide range. This work, for the first time, investigates the influence of the paste roll on fine-line printing, paste spreading and cling zone formation. It correlates the fine-line screen printing behavior of pastes to their rheological properties, e.g., yield stress, shear viscosity, and elongation flow resistance, which can be determined using standard rheological equipment and carefully chosen experimental protocols.<sup>25</sup> This combination of printing process analysis and comprehensive rheological characterization is considered to provide valuable insights for future development of fine-line screen-printable pastes. ZnO is a semi-conductive material frequently used in screen-printable pastes, e.g., for varistors<sup>26–28</sup> or as transparent conductive layers in thin-film solar cells.<sup>29,30</sup> Here, ZnO pastes have been selected not only because of their technical relevance in printed electronics. These pastes also have well-defined, conventionally accessible rheological properties, enabling straightforward correlation to printing performance. In contrast, rheological characterization of silver pastes, e.g., used for front-side metallization of Si-solar cells, can be very challenging due to wall slip and spillage phenomena occurring during rheological testing.<sup>25</sup> Moreover, wall slip and wetting phenomena can play a critical role in screen printing depending on continuous phase composition in a subtle manner. Here we wanted to avoid this additional degree of complexity. The model ZnO pastes prepared here are not prone to wall slip on the investigated length scale.

## Materials and preparation

Six pastes were prepared using zinc oxide particles (ZnO, Zinc Oxid Pharma 4, Grillo Zinkoxid GmbH) as solid phase with an average diameter  $x_{50} \approx 0.66$   $\mu\text{m}$  and a density  $\rho \sim 3.6$  g/cm<sup>3</sup>.

The dispersant, DISPERBYK-180 (a commercial dispersant including an alkylol ammonium salt of an acidic copolymer from BYK Additives & Instruments), was used to promote de-agglomeration and stabilization of the ZnO particles. Texanol (trimethyl hydroxypentyl isobutyrate,  $\rho = 0.95$  g/cm<sup>3</sup>; boiling point  $\sim 244^\circ\text{C}$ ; Sigma-Aldrich) was used as solvent,<sup>31–33</sup> and polymer binder either ethyl cellulose (ETHOCEL Std. 4 or EC N4,  $\rho \sim 1.13$  g/cm<sup>3</sup>, The Dow Chemical Company),<sup>34–37</sup> or Thixatrol Max (T-Max, organic thixotrope based on specific diamide wax,  $\rho = 1.02$  g/cm<sup>3</sup>, Elementis Specialties, Inc.)<sup>38,39</sup> were added at

different concentrations to vary flow properties systematically. Both organic additives are commonly used in screen printing formulations and are used here without further treatment.

Table 1 lists the detailed composition of the six pastes. The solid, dispersant, and solvent are almost identical for all pastes, but with different types and concentrations of rheological additive. The pastes are labeled referring to the concentration of additives ( $C_{\text{additive}}$ ) in corresponding organic medium, e.g., EC 9.5 means the paste formulated with the medium including 9.5 wt% ethyl cellulose dissolved in Texanol.

Figure 1 shows the sample preparation procedure. Samples 1–3 were formulated with different concentrations of ethyl cellulose in Texanol ( $C_{\text{EC}}$ ) as so-called organic mediums. Ethyl cellulose powder was mixed with Texanol at 60°C for 30 min until fully dissolved. The ZnO particles were initially mixed with dispersant and the prepared ethyl cellulose/Texanol solution in a porcelain bowl and then milled using a three roll mill (EXAKT E80, EXAKT Advanced Technologies GmbH) to get a homogenous paste. The rotation speed was 150 rpm and the gaps were 50–40, 40–30, 30–20, 20–10, 10–5, and 5–5  $\mu\text{m}$  for six subsequent milling steps, respectively.

Samples 4–6 were prepared with different concentrations of Thixatrol Max in Texanol ( $C_{\text{T-Max}}$ ). Thixatrol Max powder was mixed with Texanol using a rotational dissolver (Dissolver DISPERMAT® CV-PLUS, VMA-Getzmann GmbH) for 15 min at 200 rpm under room temperature and then heated up

to 65°C in a water bath and further mixed for 30 min at 1000 rpm. Finally, the solution was allowed to cool down to room temperature while stirred at 200 rpm. This high temperature and high shear process activates Thixatrol Max to form a sample spanning network in the solvent.<sup>40</sup> The remaining steps for samples 4–6 were the same as in the preparation for samples 1–3.

## Experiments

### Rheological measurements

Several rheological tests were employed to characterize the pastes, including yield stress measurement, flow curve determination, three-interval thixotropic test (3ITT), and filament stretching test. The yield stress was measured as described in reference (19) using a rotational rheometer (Haake MARS from Thermo Fisher Scientific) a vane ( $d = 10 \text{ mm}$ )-in-cup ( $d = 20 \text{ mm}$ ) geometry at 23°C and evaluating the deformation vs shear stress data according to the tangent intersection method. Flow curve was measured in the shear rate range from 1 to 1000  $\text{s}^{-1}$  with 10 points/decade and 1-s sampling time for each point using a rotational rheometer (MCR 302 from Anton Paar) with plate–plate geometry ( $d = 25 \text{ mm}$ ) at a gap height of 0.5 mm at 23°C. The three-interval thixotropic test<sup>41</sup> was performed using the same setup as for the flow curve. The shear rates were 1, 500, and 1  $\text{s}^{-1}$

**Table 1: Pastes composition**

Label	EC 9.5	EC 7.5	EC 5.5	T-Max 9.5	T-Max 7.5	T-Max 5.5
Texanol (wt%)	9.22	9.24	9.26	9.22	9.24	9.26
EC N4 (wt%)	0.97	0.75	0.54	–	–	–
Thixatrol Max (wt%)	–	–	–	0.97	0.75	0.54
ZnO (wt%)	87.20	87.39	87.58	87.20	87.39	87.58
DISPERBYK 180 (wt%)	2.61	2.61	2.62	2.61	2.61	2.62

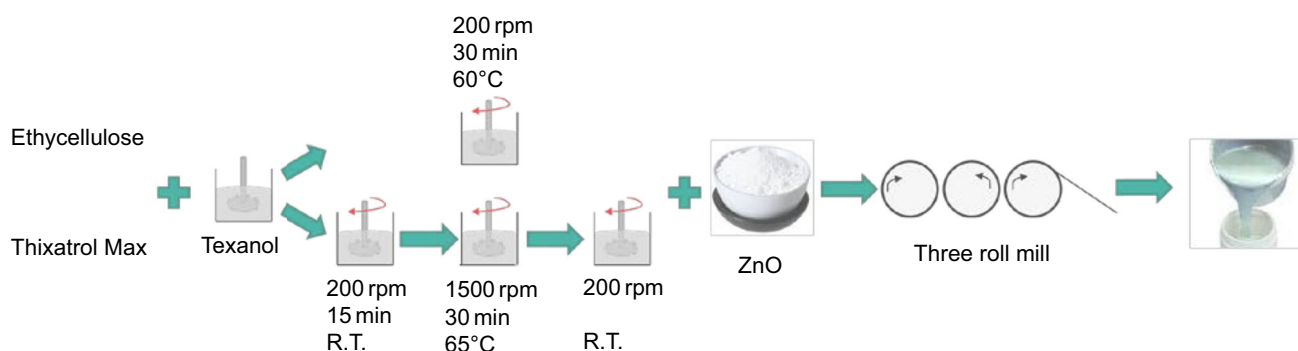


**Fig. 1: Processing route for preparing ethyl cellulose and Thixatrol Max mediums as well as subsequent addition of ZnO and milling of the mixture to obtain homogenous pastes**

acting on the sample for 120, 2, and 360 s during the three intervals.<sup>38</sup> The pastes investigated here do not exhibit significant wall slip as confirmed by changing the measuring gap height. Filament stretching tests were performed using a Capillary Breakup Elongational Rheometer (CaBER1, Thermo Fisher Scientific) with two plates of 6 mm in diameter. The paste was placed between these plates at a gap of 1 mm. Then the upper plate was vertically moved with a separation speed of 2 mm/s, thus creating and stretching a paste filament. A high-speed camera (Photron FastCam-X1024 PCI) was used to monitor filament deformation and break. More information about the test protocol can be found.<sup>25</sup>

### High-speed video imaging of the screen printing process

Figure 2 illustrates the setup of the screen printing system. A commercial screen printer (EKRA E2, ASYS Group) was modified by removing the transporting and optical positioning systems and keeping the print head and screen clamping. A high-speed camera (MotionBLITZ EoSens<sup>®</sup> mini, Mikrotron GmbH) with an objective (Olympus LMPLFLN 10X) was inserted to capture motion of the paste, squeegee and screen as well as paste flow at a frame rate of 1000 fps and resolution of  $1708 \times 832$  pixels,  $\sim 0.75 \mu\text{m}/\text{pixel}$  below the substrate.

The vacuum table is designed as in Fig. 2, with an open area in the middle for direct investigation from the bottom. A transparent glass plate (1 mm thickness, window glass), which is strong enough to withstand the squeegee pressure, was placed on the movable substrate table.

The squeegee position was identified by the sharp pattern of the screen on the substrate due to the high pressure acting by the squeegee (see Fig. 2a). Due to the deformation, the contact between the squeegee and substrate is not a contact line but a finite contact area (nip-contact in Fig. 2a). A similar but less sharp pattern was also observed in the region where the screen was in contact with the substrate due to paste stickiness. The rear end of this pattern is the snap-off point (see Fig. 2b). The paste was observed by the reflection of the light (black part). With the positions of the paste and the squeegee, we can determine the pre-injection zone (Fig. 2a): The area ahead of the squeegee where the paste is already pushed through the screen opening due to the shear stress in the paste roll on the screen  $p_{\text{screen}}$ . The length of the pre-injection zone is determined by the distance between the first paste dot on the substrate and contact point between squeegee and screen (nip-contact). Residual paste remains on the screen after the first printing cycle and deteriorates the determination of the pre-injection zone length. Therefore, we only collected data ob-

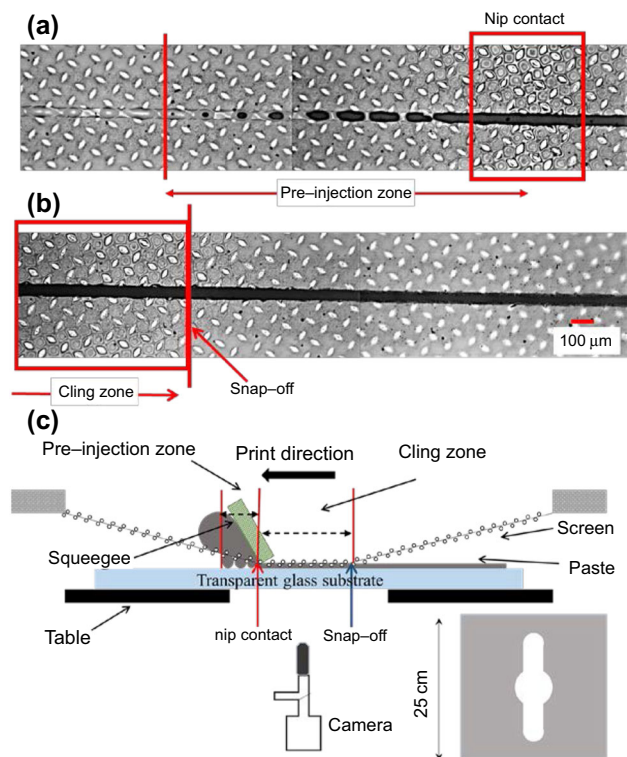


**Fig. 2:** (a) Image of nip-contact and pre-injection zone. The nip-contact (the contact area between the squeegee and screen) is indicated by the pattern in the rectangle. This kind of pattern is not visible in the left part of the picture. Two pictures have been combined to show the pre-injection zone. (b) Image of snap-off point. The rectangle indicates the “less sharp” pattern designating the region where the mesh sticks to the substrate. This kind of pattern is not visible in the right of the picture. Two pictures have been put together to show the difference between the area where the screen contacts the substrate and where the screen has left from the substrate. The boundary indicates the point where the screen loses contact with the screen. The scale bar applies to both pictures. Both figures (a) and (b) have been processed to increase contrast and sharpness for better visibility. More information (high-speed video imaging series) can be found in the supplementary material. (c) The schematic of the equipment and the design of the vacuum table

served in the first print cycle with a clean screen. With the nip-contact and snap-off point, the cling zone is determined.

Paste spreading has been investigated by observing paste-covered areas over time. The printed electrode geometry is influenced by the screen opening direction.<sup>42</sup> Therefore, two different positions were observed: the busbar/finger connection area, with screen opening perpendicular to the printing direction, and a fine-line area, with screen opening parallel to the printing direction.

Commercial screens and typical printing parameters were used to mimic the technical case, i.e., front-side

silver paste printing on Si-solar cells as close as possible. Figure 3 schematically shows the printed pattern used in this study. Tables 2, 3, and 4 list the detailed technical parameters of the used screen, the pattern parameters, and the printing parameters used in this study. 95 g of the paste is placed on the screen for each sample.

After the investigation of the printing process using the high-speed camera, the pastes were screen printed onto mono-crystalline silicon wafers, for printed electrode width determination using a 3D light microscope (VHX-600, Keyence Corp., Neu-Isenburg, Germany). Six lines are analyzed at different positions on the wafer. *ImageJ* was used to transfer the original microscopic images to binarized pictures (Fig. 4). There are 1600 pixels in the horizontal direction. Therefore, 1600 width data are extracted and averaged from one picture; in total the average width and the standard deviation values discussed below are calculated from 9600 individual data. Due to the periodic change of the screen pattern, the printed electrode width changes correspondingly, resulting in a large standard deviation of width data. However, the average value is still a statistically suitable parameter reflecting the shaded line width on the surface. The average values of the line width data for the six pastes are related to rheological properties in the discussion part below.

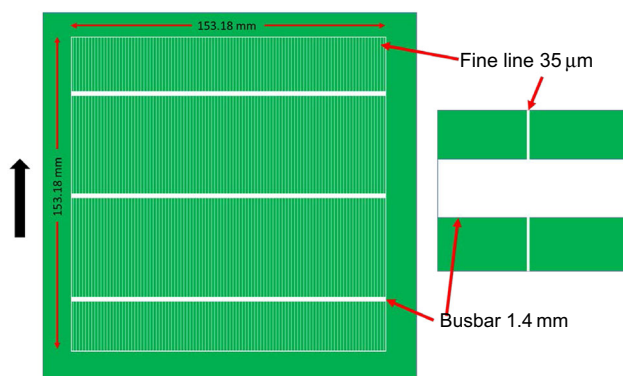


**Fig. 3: Schematic of the screen design.** The green part is the area covered by the polymer film and the white area is the screen opening. There are 102 fine lines with constant width of 35  $\mu\text{m}$  and 3 busbars with constant width of 1.4 mm. The black arrow indicates the printing direction. The scheme on the right is a close-up of the intersection between a busbar and a fingerline (Color figure online)

## Results and discussion

### Rheological properties of pastes

#### Yield stress

All investigated pastes exhibit an apparent yield stress  $\sigma_y$ , i.e., a minimum stress required to force the pastes to flow. Stress ramp experiments covering the shear stress range from 10 to 10,000 Pa were employed, and the tangent method was applied to determine  $\sigma_y$  from the corresponding deformation  $\gamma$  vs shear stress  $\sigma$  data. The yield stress  $\sigma_y$  is plotted vs additive concentration ( $C_{\text{additive}}$ ), and a typical  $\gamma \sim \sigma$  curve is shown as an insert in Fig. 5. This quantity linearly increases with increasing  $C_{\text{additive}}$  for both sample series. But at a given  $C_{\text{additive}}$ , the Thixatrol Max samples exhibit a higher  $\sigma_y$  than those based on ethyl cellulose (see Fig. 5). The thixotropic agent forms a strong, sample spanning structure due to thermal activation under high shear and high temperature during organic medium preparation.<sup>40</sup> It is further reinforced by the added ZnO particles. This network increases the overall viscosity and  $\sigma_y$ , thus avoiding bulk phase separation and guaranteeing long shelf life.<sup>43</sup> On the other hand, ethyl cellulose is molecularly dissolved in Texanol, resulting in a strong increase in viscosity and also introducing weak shear thinning (data not shown here). Attractive van der Waals and/or depletion interaction among added ZnO particles results in a yield stress and a strong degree of shear thinning compared to the solution (see next section).

**Table 3: Pattern parameters used in this study**

Fine-line opening	No. of fine lines	Busbar opening	No. of busbars
35 $\mu\text{m}$	102	1.4 mm	3

**Table 4: Printing parameters used in this study**

Printing speed	Flooding speed	Snap-off	Pressure
300 mm/s	400 mm/s	1.6 mm	75 N/cm

**Table 2: Technical parameters of the screen used in this study**

Mesh no.	Thread diameter	Fabric thickness	Tension
360 l/inch	16 $\mu\text{m}$	22 $\mu\text{m}$	$26 \pm 2 \text{ N}\cdot\text{cm}^{-1}$
EOM	Angle between mesh and fine-line opening		
17 $\mu\text{m}$	30°		

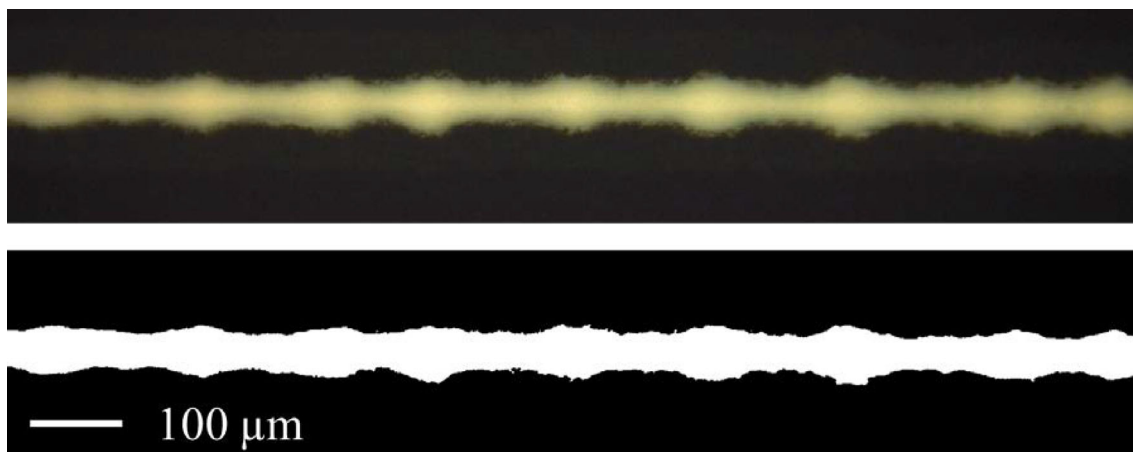


**Fig. 4:** The original microscopic (top) and binarized (bottom) images. There are 1600 pixels in the horizontal direction. Therefore, 1600 line width data are collected from one image. The printed electrode width changes due to the influence of the periodic change of the screen mesh

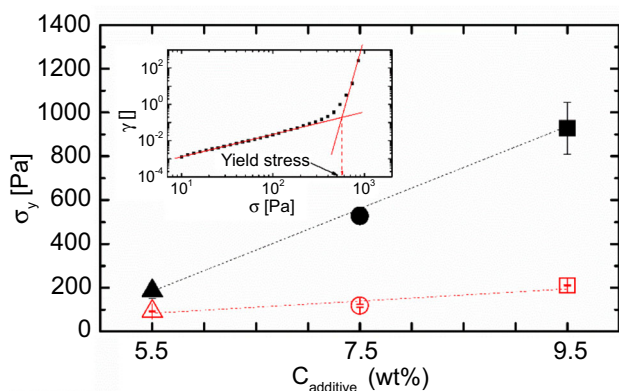


**Fig. 5:** Yield stress vs Thixatrol Max (solid points) and ethyl cellulose (open points) concentration, respectively. The inserted figure is a typical  $\gamma$ - $\sigma$  curve for yield stress determination based on the tangent intersection method

#### Flow curve

The viscosity of the six pastes  $\eta$  with different types and concentrations of additives was measured in the shear rate range between 1 and 1000  $\text{s}^{-1}$ . All pastes clearly show a power-law-type shear thinning behavior  $\eta \sim \dot{\gamma}^{n-1}$  (see Fig. 6). The degree of shear thinning is characterized by the exponent  $n$ , which is obtained from fitting the above power-law relationship to the experimental data shown in Fig. 6. Corresponding values for the six investigated samples are listed in Table 3 together with other rheological parameters. The pastes with Thixatrol Max show more pronounced shear thinning ( $n < 0.25$ ), than the pastes with ethyl cellulose ( $n \sim 0.50$ ). This distinctly different signature of flow curves can be rationalized as follows: The sample spanning network provided by Thixatrol Max results in a high viscosity at low shear rate but rapidly

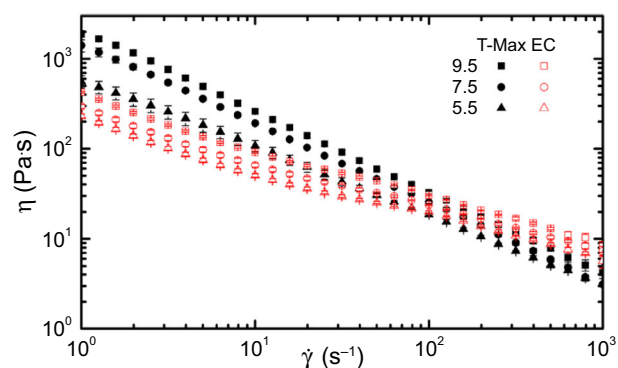


**Fig. 6:** Flow curves for six pastes with Thixatrol Max (solid points) and ethyl cellulose (open points) concentrations, respectively

breaks down under moderate high external forces. In contrast, the ethyl cellulose dissolved on a molecular level preserves a high viscosity level even under high shear. The flow curves of the two series cross each other in the shear rate range between 75 and 150  $\text{s}^{-1}$ .

#### Thixotropy

Structural and viscosity recovery of the pastes after high shear was characterized using the 3ITT with 1, 500, and 1  $\text{s}^{-1}$  for 120, 2, and 360 s. The pastes' viscosity gradually recovers after cessation of the high shear treatment. This viscosity recovery in the third interval of the test can be described very well by an exponential equation:  $\eta_3(t) = \eta_f + A \cdot \exp(-t/\tau)$  (see insert in Fig. 7), where the time constant  $\tau$  characterizes the recovery rate. In Fig. 7, this quantity is shown vs additive concentration. For both additives, structure recovers faster at higher  $C_{\text{additive}}$ , and generally recov-

ery is faster for the ethyl cellulose system than for the Thixatrol Max system.

Moreover, the 3ITT revealed that the structure irreversibly changes during exposure to high shear in the second interval. This effect is characterized by the ratio of the viscosities obtained in the third and first intervals. These values are summarized together with other characteristic rheological data in Table 5. For both additives, viscosity recovers to a higher extent at lower  $C_{\text{additive}}$  and generally pastes recovery is more pronounced for the ethyl cellulose system than for the Thixatrol Max system. The damage of the network formed by thixotropic agent is obviously irreversible, at least on a technically relevant time scale  $\sim 1$  h. Viscosity values recorded in the second interval at a shear rate of  $500 \text{ s}^{-1}$  and time constant  $\tau$  data are also summarized in Table 5.

Finally, it should be mentioned that due to hardware and software constraints of our commercial rheometer, it takes at least 400 ms to reach a steady shear rate in the third interval and this test may not be appropriate to characterize fast printing and spreading processes as

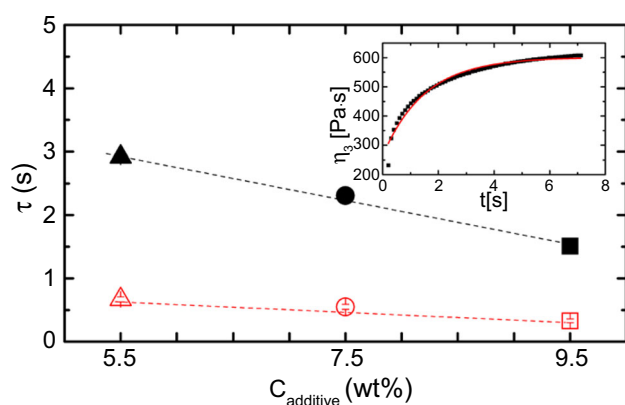


**Fig. 7:** Time constant  $\tau$  vs Thixatrol Max (solid points) and ethyl cellulose (open points) concentration. The inserted figure is a typical viscosity recovery curve after cessation of high shear in the third interval. The red line is the simulated curve using an exponential equation:  $\eta_3(t) = \eta_t + A \exp(-t/\tau)$  (Color figure online)

will be discussed in the “Printed electrode width” section.

#### Elongational breakup of pastes

The paste stickiness prevents separation of the screen from the substrate after the squeegee has passed. Filament stretching test has been performed to simulate the paste breakup at the snap-off point. The fracture strain  $\varepsilon$  in this experiment is defined as  $\varepsilon = (h_f - h_0)/h_0$ , where  $h_0$  is the initial gap height and  $h_f$  is the gap height at which the filament breaks, as observed from video imaging. The pastes with ethyl cellulose show higher  $\varepsilon$  than the pastes with thixotropic agent (see Fig. 8). The fracture strain  $\varepsilon$  increases with  $C_{\text{EC}}$  but decreases with  $C_{\text{T-Max}}$ . The dissolved ethyl cellulose increases continuous phase viscosity and paste cohesion, thus stabilizing the stretched filament and resulting in a larger  $\varepsilon$ . This effect increases with increasing  $C_{\text{EC}}$ . In contrast, the pastes which contain thixotropic agent exhibit weak internal cohesion and brittle failure, receiving their elasticity from a sample

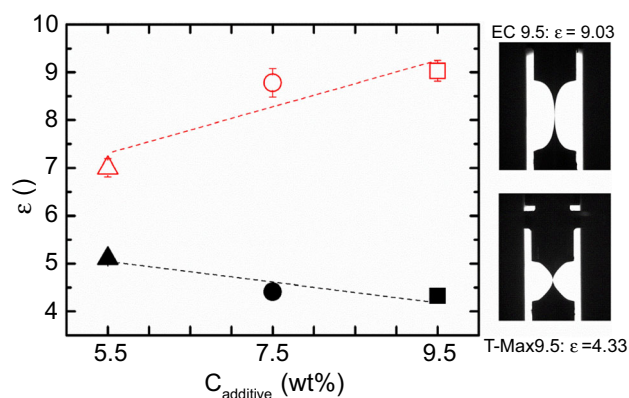


**Fig. 8:** Fracture strain  $\varepsilon$  vs Thixatrol Max (solid points) and ethyl cellulose (open points) concentration, respectively. The inserted figures illustrate the filament breakup for pastes EC 9.5 (upper figure) and T-Max 9.5 (bottom figure), respectively

**Table 5:** Summary of rheological data of six pastes

	T-Max 9.5	T-Max 7.5	T-Max 5.5	EC 9.5	EC 7.5	EC 5.5
Yield stress $\sigma_y$ (Pa)	$928 \pm 118$	$528 \pm 22$	$186 \pm 34$	$211 \pm 2$	$118 \pm 7$	$92 \pm 2$
Power-law index $n$	$0.11 \pm 0.03$	$0.10 \pm 0.02$	$0.23 \pm 0.02$	$0.46 \pm 0.04$	$0.50 \pm 0.03$	$0.51 \pm 0.03$
Viscosity $\eta_{\text{low}}$ at $1 \text{ s}^{-1(\dagger)}$ (Pa·s)	$1550 \pm 80$	$1017 \pm 19$	$573 \pm 24$	$334 \pm 3$	$244 \pm 2$	$161 \pm 2$
Viscosity $\eta_{\text{high}}$ at $500 \text{ s}^{-1(\dagger)}$ (Pa·s)	$7.1 \pm 0.5$	$5.3 \pm 0.1$	$4.5 \pm 0.3$	$14.8 \pm 0.6$	$12.3 \pm 0.2$	$9.0 \pm 0.8$
Ratio of viscosity in third over first interval $\eta_3/\eta_{\text{low}}^{(\dagger)}$ (%)	$45.0 \pm 1.7$	$48.0 \pm 0.5$	$54.0 \pm 4.6$	$62.6 \pm 2.7$	$84.9 \pm 1.0$	$89.9 \pm 0.1$
Recovery time constant $\tau^{(\dagger)}$ (s)	$1.51 \pm 0.07$	$2.31 \pm 0.09$	$2.92 \pm 0.09$	$0.33 \pm 0.03$	$0.55 \pm 0.04$	$0.67 \pm 0.04$
Fracture strain $\varepsilon$	$4.33 \pm 0.07$	$4.41 \pm 0.12$	$5.11 \pm 0.07$	$9.03 \pm 0.22$	$8.78 \pm 0.30$	$7.0 \pm 0.19$

( $\dagger$ ) data derived from 3ITT

spanning network formed in activation but immediately breaking down upon elongation. Figure 8 shows exemplarily the broken filaments for pastes EC 9.5 and T-Max 9.5, respectively. Obviously, the filament formed with ethyl cellulose paste is longer, similar to slender cylindrical filaments formed with polymer solution in conventional CaBER tests.<sup>44</sup> In contrast, the pastes including Thixatrol Max break with a neck shape, typically for yield stress fluids.<sup>45</sup>

### Correlation of printing process features and rheological paste rheological properties

#### Pre-injection zone

The length of the pre-injection zone formed during screen printing was determined from image analysis for all six pastes as described in the “High-speed video imaging of the screen printing process” section. Obviously, there is a linear relationship between pre-injection length,  $l_{pi}$  and the reciprocal of yield stress,  $1/\sigma_y$  (see Fig. 9). As mentioned above, the shear stress acting on the paste roll ahead of the printing squeegee has been calculated to decrease reciprocally with the distance to the squeegee assuming Newtonian as well as shear thinning behavior of the pastes.<sup>20-22</sup>

The paste is squeezed through the screen only when this pressure exceeds  $\sigma_y$  and, accordingly,  $l_{pi}$  increases with  $1/\sigma_y$ , irrespective of the type and concentration of the rheological additives.

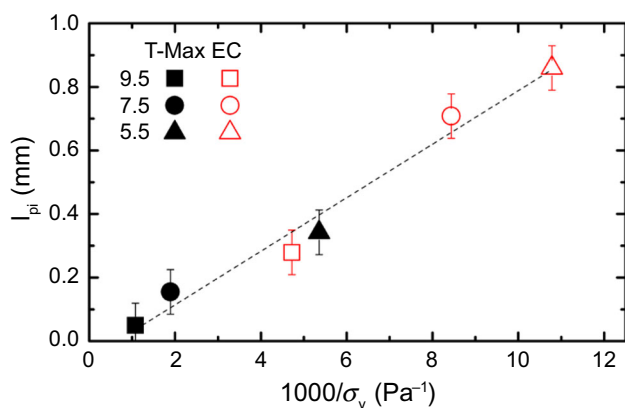


**Fig. 9:** Pre-injection length  $l_{pi}$  vs the reciprocal of yield stress  $1000/\sigma_y$  for six pastes with different concentrations of Thixatrol Max (solid points) and ethyl cellulose (open points). The line indicates the linear relationship between  $l_{pi}$  and  $1000/\sigma_y$ . The error bar is estimated as half the width of the deformed squeegee. The low  $l_{pi}$  value formed for paste with T-Max 9.5 means the paste is pushed on the substrate only right under the printing squeegee rather than in the paste roll ahead considering the deformation of the squeegee

#### Cling zone

As described above, the cling zone length  $l_{cl}$  is given by the distance between the nip-contact and the snap-off position and has also been determined from the different pictures in the video sequence. The relationship between the cling zone length  $l_{cl}$  and fracture strain  $\epsilon$ , as obtained from the filament stretching experiment, is essentially linear irrespective of the type of additive included in the pastes (see Fig. 10),  $l_{cl}$  increases with  $C_{EC}$  but decreases with  $C_{T-Max}$ . The pastes including ethyl cellulose exhibit a much longer  $l_{cl}$  than the Thixatrol Max-modified pastes. The ethyl cellulose polymer dissolved in the continuous phase on a molecular disperse level provides a weak viscoelastic paste behavior with its characteristic internal cohesion and extended stretchability finally holding the screen attached to the substrate for a long time before it snaps off. On the other hand, the pastes including Thixatrol Max exhibit short breakup length, weak internal cohesion, and brittle failure typical for particulate gels, receiving their elasticity from a sample spanning network, e.g., of microgel particles.<sup>46</sup> Such gels fail at low critical deformation and thus release the screen from the substrate easily, hence resulting in a short  $l_{cl}$ .

#### Paste spreading

Paste spreading is an important parameter, determining the final geometrical dimensions of a printed pattern. Here we have analyzed this printing phenomenon directly employing high-speed video imaging. Behavior of all six pastes has been investigated at two characteristic positions, namely in the busbar/finger connection area as well as in the fine-line area.

Spreading of the T-Max 5.5 paste in the busbar/finger connection area is shown in Fig. 11. The sequence of binarized images, taken within the first 100 ms after the squeegee had passed the observed area, is displayed in Fig. 11a, clearly showing the spreading of the paste. We have binarized these images

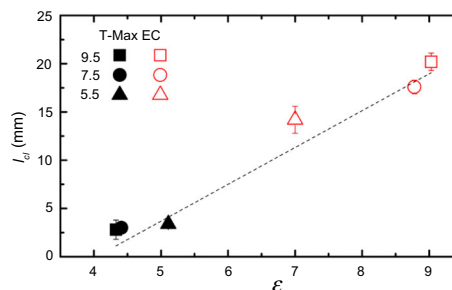


**Fig. 10:** Cling zone length  $l_{cl}$  vs fracture strain  $\epsilon$  in filament stretching test for six pastes with different concentrations of Thixatrol Max (solid points) and ethyl cellulose (open points). The line indicates the approximately linear relationship between  $l_{cl}$  and  $\epsilon$

from the original images (see Figs. 11b, 11c) and counted the number of black pixels as a measure for the area occupied by the paste. The paste occupied area at time  $t$  ( $A_t$ ) is normalized with occupied area at time  $t = 0$  ( $A_{t=0}$ ), where  $t = 0$  means the squeegee had just passed the observed area. The time evolution of this quantity characterizes the spreading kinetics and the data presented in Fig. 11d and clearly demonstrates

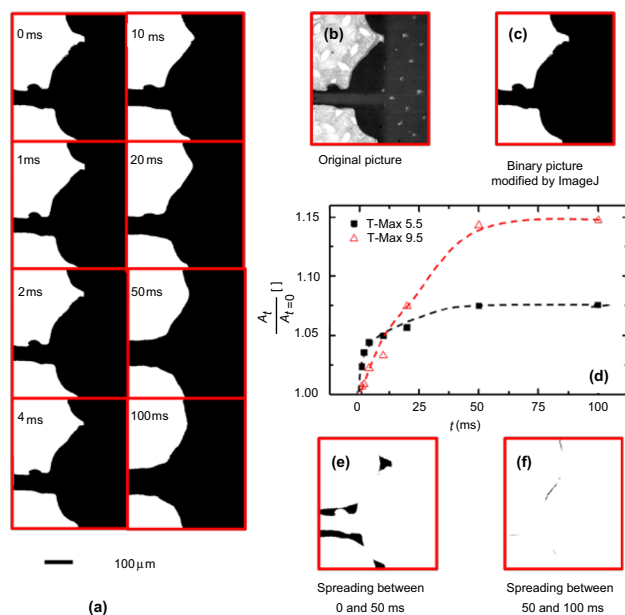


**Fig. 11: Spreading of the paste including 5.5 wt% Thixatrol Max at the intersection between busbar and fingerline. (a) Image sequence of the observed area (binary pictures). The printing direction is from right to left. Time 0 ms means the squeegee had just passed the observed area. (b) The original image of the observed area at time  $t = 0$  ms used for binarization. (c) The binarized image from the original figure shown in (b). The change in normalized area covered with paste is shown in (d) where  $A_t/A_{t=0}$  is plotted vs time.  $A_t$  and  $A_{t=0}$  refer to the paste-covered area at time  $t$  and  $t = 0$  ms, respectively. The change of covered area due to spreading can also be seen from the difference between binarized images taken at  $t = 50$  ms and  $t = 0$  ms (e) and those taken at  $t = 100$  ms and  $t = 50$  ms (f), respectively**

that paste spreading took place during the first 50 ms and was finished within 50–100 ms. The amount of spreading within the first 50 ms can be directly seen subtracting the binarized images taken at  $t = 50$  ms and  $t = 0$  ms, and the black regions visible in Fig. 11e directly show the wafer area covered due to spreading. Essentially no further increase in silver-covered area takes place within the period between  $t = 50$  ms and  $t = 100$  ms, as can be seen when subtracting the corresponding binarized images (Fig. 11f). Similar results have been obtained for all other pastes investigated here (e.g., T-Max 9.5 in Fig. 11d), without revealing a clear trend in spreading kinetics depending on the type and concentration of additives.

The time constant of thixotropic, i.e., structural recovery,  $\tau$ , for the pastes investigated here varies between 0.3 and 0.7 s for ethyl cellulose-based pastes and between 1.5 and 3 s for the pastes including Thixatrol Max according to 3ITT, which is often used to characterize this rheological feature of screen printing pastes. These long characteristic recovery times accessible with the 3ITT are apparently not relevant for the screen printing process investigated here.

On the other hand, no spreading could be observed in the fine finger region within the given range of spatial and temporal resolution of our experimental setup. It seems that the paste stopped moving and the electrode shape was fixed when the squeegee had passed a given position. Finally, we would like to mention that the pastes were pushed into the gap between the screen and the substrates. After the snap-off process, the paste in the gap was partially detached and formed a bleeding area or a fuzzy finger as hypothesized earlier.<sup>47</sup> This effect was more pronounced for pastes with lower viscosity.

### Printed electrode width

The video image analysis proves that there is no spreading after the printing squeegee has passed in the fine-line region. Therefore, the width of the printed

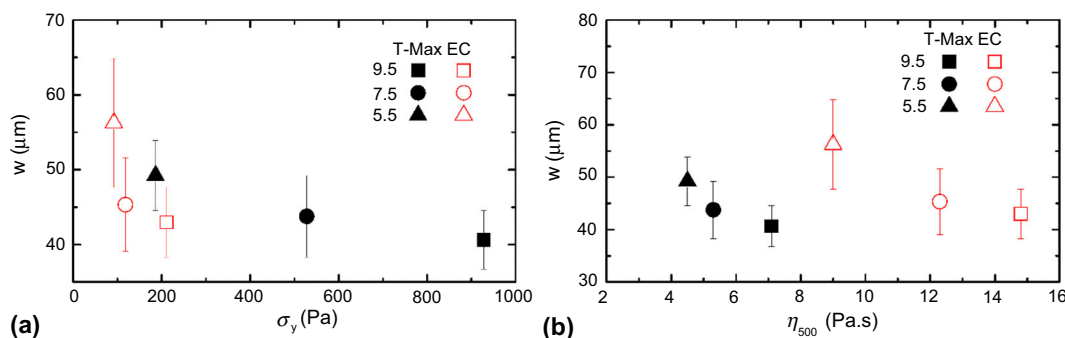


**Fig. 12: Average electrode width  $w$  vs yield stress  $\sigma_y$  (a) high shear rate viscosity  $\eta$  at  $500 \text{ s}^{-1}$  (b) and for six pastes with different concentrations of Thixatrol Max (solid points) and ethyl cellulose (open points)**

electrodes  $w$  is determined only in the pre-injection zone.

The electrode width  $w$  is analyzed from the binarized pictures processed by *ImageJ* (see Fig. 4) including 9600 data points. Higher yield stress  $\sigma_y$  reduces the electrode width  $w$  within both series (see Fig. 12a). The pastes with Thixatrol Max form narrower electrodes than the pastes with ethyl cellulose at a given  $C_{\text{additive}}$ . There is, however, no general scaling relating  $w$  and  $\sigma_y$  or length of the pre-injection zone  $l_{\text{pi}}$  valid for both types of additives. Besides  $\sigma_y$ , the high shear viscosity  $\eta_{500}$  is supposed to have an effect on  $w$  (see Fig. 12b). In previous work,<sup>38,39</sup> the characteristic shear rate in the pre-injection zone was estimated to be around  $500 \text{ s}^{-1}$ . In Fig. 12b, we display the electrode width  $w$  as a function of  $\eta_{500} = \eta(\dot{\gamma} = 500 \text{ s}^{-1})$ . For both series,  $w$  decreases with increasing  $\eta_{500}$ , i.e.,  $C_{\text{additive}}$ . But again, no general correlation between both parameters, holding for both types of rheological control additives is formed. This is not surprising since both additives contribute to the buildup of  $\sigma_y$  and  $\eta_{500}$  in a different manner, i.e., based on different physical mechanisms. At a given  $C_{\text{additive}}$ , Thixatrol Max provides a higher  $\sigma_y$  and ethyl cellulose provides a higher  $\eta_{500}$ .

The obtained printed electrode width is always higher than the screen opening. The paste spreading distance/electrode width can be estimated with a simple model:  $w \sim \int_0^{t_{\text{pi}}} v dt$ , where the  $v$  and  $t$  are moving speed and time under pressure, respectively.  $t_{\text{pi}}$  is determined by  $l_{\text{pi}}$  over printing speed  $V_{\text{print}}$  and speed  $v$  is inversely proportional to viscosity. This simple scaling model suggests a linear relationship between  $w$  and  $(\sigma_y \eta_{500})^{-1}$ . Replotting the above data accordingly nicely confirms this crude approximation as shown in Fig. 13. Finally, it should be pointed out

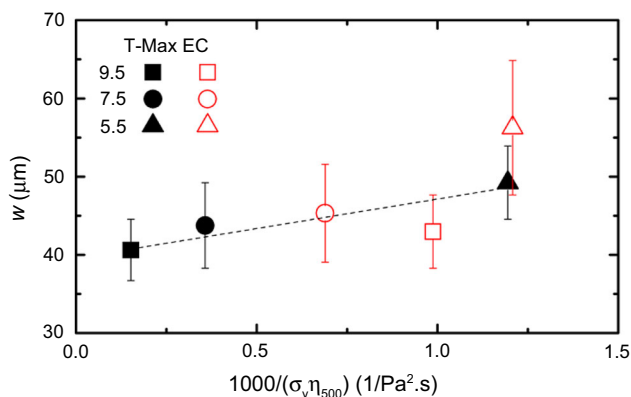


**Fig. 13: Electrode width  $w$  vs the reciprocal of product of yield stress and high shear viscosity  $1000/(\sigma_y \eta_{500})$  for six pastes with different concentrations of Thixatrol Max (solid points) and ethyl cellulose (open points). The dashed line corresponds to a linear fit to the experimental data yielding a regression coefficient  $R^2 = 0.59$ . For comparison: fitting a horizontal line, i.e., assuming that the line width is independent of these rheological data resulted in  $R^2 = 0.15$**

that both additives contribute to the control of the electrode width based on different physical mechanisms and hence they may be combined in more sophisticated paste recipes to achieve a further reduction in electrode width.<sup>42</sup>

## Conclusions

Six model pastes, with different types (binder and thixotropic agent) and concentrations (9.5, 7.5, and 5.5 wt% in medium) of rheological additives, have been prepared and their rheological properties have been characterized including yield stress  $\sigma_y$ , flow curve  $\eta(\dot{\gamma})$ , viscosity recovery time  $\tau$  after high shear treatment as determined in three-interval thixotropic test, and filament deformation at failure as determined in the uniaxial filament stretching test. Due to the sample spanning network formed during thermal activation, the pastes with Thixatrol Max show significantly higher yield stress ( $\sigma_y \sim 180\text{--}980 \text{ Pa}$ ) than those with ethyl cellulose ( $\sigma_y \sim 98\text{--}206 \text{ Pa}$ ). On the other hand, the pastes with ethyl cellulose are more viscous at high shear rate, since this additive is molecularly dispersed in the solvent. These different thickening mechanisms also show up during filament stretching, and generally ethyl cellulose-based pastes exhibit at higher fracture strain than pastes including Thixatrol Max. Finally, thixotropic recovery after high shear happens distinctly faster for the ethyl cellulose system than for Thixatrol Max-based systems.

The model pastes have been printed on a transparent glass plate, and a high-speed camera was used to record the motion of the squeegee, screen, and paste. The length of the pre-injection zone, where the paste is pushed through the screen opening, is controlled by the yield stress. Since the stress decreases inversely proportional to the distance from the squeegee, the length over which this stress exceeds the yield stress scales as  $l_{\text{pi}} \sim 1/\sigma_y$ , irrespective of the type of rheological control agent, as confirmed by our experimental results. The length of cling zone  $l_{\text{cl}}$ , where the screen clings on the substrate, increases with paste stickiness, characterized here by the fracture strain  $\varepsilon$  determined from filament stretching experiments. Here, we found a linear relationship  $l_{\text{cl}} \sim \varepsilon$  with a pre-factor valid for both types of additives.

Paste spreading could be detected at the busbar/finger connection area and turned out to happen very fast within 50–100 ms after the squeegee had passed, irrespective of paste composition. The 3ITT performed on commercial rotational rheometers is not capable of capturing structural recovery phenomena on such short-time scales. Moreover, the structural recovery times determined in this test are on the orders of seconds and thus seem not to be relevant for the screen printing process investigated here. In the fine-line area, no significant spreading was detectable with our experimental setup. Accordingly, we conclude that

the width of the electrode is determined in the pre-injection zone.

The decisive mechanisms are: first, penetration of paste through the screen opening ahead of the squeegee; second, the flow of the paste in the pre-injection period. The former is related to  $\sigma_y$  and the latter to  $\eta_{500} = \eta$  ( $\dot{\gamma} = 500 \text{ s}^{-1}$ ) and accordingly as  $w \sim 1/(\sigma_y \eta_{500})$  as expected from a crude estimation  $w = \int_0^{t_{pi}} v dt$ .

**Acknowledgments** The authors would like to acknowledge support from BASF SE, especially the fruitful discussion with Dr. H. Dietsch and the technical support from M. Machate and B. Strubel for setting up the screen printer.

## References

- Ostfeld, AE, Deckman, I, Gaikwad, AM, Lochner, CM, Arias, AC, "Screen Printed Passive Components for Flexible Power Electronics." *Sci. Rep.*, **5** 15959 (2015)
- Eshkeiti, A, Reddy, ASG, Emamian, S, Narakathu, BB, Joyce, M, Joyce, M, Fleming, PD, Bazuin, BJ, Atashbar, MZ, "Screen Printing of Multilayered Hybrid Printed Circuit Boards on Different Substrates." *IEEE Trans. Compon. Packag. Manuf. Technol.*, **5** (3) 415–421 (2015)
- Kim, JH, Kim, J, Lee, GJ, Jeong, J, Choi, B, "Screen-Printed Cu Source/Drain Electrodes for a-InGaZnO Thin-Film Transistors." *Mol. Cryst. Liq. Cryst. Sci. Technol.*, **586** (1) 161–167 (2013)
- Tam, SK, Fung, KY, Ng, KM, "Copper Pastes Using Bimodal Particles for Flexible Printed Electronics." *J. Mater. Sci.*, **51** (4) 1914–1922 (2016)
- Schwanke, D, Pohlner, J, Wonisch, A, Kraft, T, Geng, J, "Enhancement of Fine Line Print Resolution Due to Coating of Screen Fabrics." *J. Microelectron. Electron. Packag.*, **6** (1) 13–19 (2009)
- Faddoul, R, Reverdy-Bruas, N, Blayo, A, "Formulation and Screen Printing of Water Based Conductive Flake Silver Pastes onto Green Ceramic Tapes for Electronic Applications." *Mater. Sci. Eng. B Adv.*, **177** (13) 1053–1066 (2012)
- Wehmeier, N, Nowack, A, Lim, B, Brendemühl, T, Kajari-Schröder, S, Schmidt, J, Brendel, R, Dullweber, T, "21.0%-Efficient Screen-Printed n-PERT Back-Junction Silicon Solar Cell with Plasma-Deposited Boron Diffusion Source." *Sol. Energy Mater. Sol. Cells*, **158** 50–54 (2016)
- Kumar, P, Pfeffer, M, Willsch, B, Eibl, O, Koduvelikulathu, LJ, Mihailetchi, VD, Kopecek, R, "N-Type Single-Crystalline Si Solar Cells: Front Side Metallization for Solar Cells Reaching 20% Efficiency." *Sol. Energy Mater. Sol. Cells*, **157** 200–208 (2016)
- Phillips, C, Al-Ahmadi, A, Potts, SJ, Claypole, T, Deganello, D, "The Effect of Graphite and Carbon Black Ratios on Conductive Ink Performance." *J. Mater. Sci.*, **52** (16) 9520–9530 (2017)
- Zhang, LJ, Liu, TF, Liu, LF, Hu, M, Yang, Y, Mei, AY, Han, HW, "The Effect of Carbon Counter Electrodes on Fully Printable Mesoscopic Perovskite Solar Cells." *J. Mater. Chem. A*, **3** (17) 9165–9170 (2015)
- Schubert, G, Huster, F, Fath, P, "Physical Understanding of Printed Thick-Film Front Contacts of Crystalline Si Solar Cells—Review of Existing Models and Recent Developments." *Sol. Energy Mater. Sol. Cells*, **90** (18–19) 3399–3406 (2006)
- Li, C-W, Chuang, H-C, Li, S-T, "Hedonic Analysis for Consumer Electronics Using Online Product Reviews." *Proc. Advanced Applied Informatics (IIAI-AAI), 2016 5th IIAI International Congress on*, 2016
- Fellmeth, T, Clement, F, Biro, D, "Analytical Modeling of Industrial-Related Silicon Solar Cells." *IEEE J. Photovolt.*, **4** (1) 504–513 (2014)
- Lin, HW, Chang, CP, Hwu, WH, Ger, MD, "The Rheological Behaviors of Screen-Printing Pastes." *J. Mater. Process. Technol.*, **197** (1–3) 284–291 (2008)
- Lin, J, Wang, C, "Effects of Surfactant Treatment of Silver Powder on the Rheology of Its Thick-Film Paste." *Mater. Chem. Phys.*, **45** (2) 136–144 (1996)
- Rane, SB, Seth, T, Phatak, GJ, Amalnerkar, DP, Das, BK, "Influence of Surfactants Treatment on Silver Powder and Its Thick Films." *Mater. Lett.*, **57** (20) 3096–3100 (2003)
- Hoorstra, J, Weeber, AW, De Moor, HH, Sinke, WC, The Importance of Paste Rheology in Improving Fine Line, Thick Film Screen Printing of Front Side Metallization. Netherlands Energy Research Foundation ECN, (1997)
- Zhou, Y, Tong, H, Liu, Y, Yuan, S, Yuan, X, Liu, C, Zhang, Y, Chen, G, Yang, Y, "Rheological Effect on Screen-Printed Morphology of Thick Film Silver Paste Metallization." *J. Mater. Sci. Mater. Electron.*, **28** (7) 5548–5553 (2017)
- Xu, CH, Fiess, M, Willenbacher, N, "Impact of Wall Slip on Screen Printing of Front-Side Silver Pastes for Silicon Solar Cells." *IEEE J. Photovolt.*, **7** (1) 129–135 (2017)
- Riemer, DE, "The Theoretical Fundamentals of the Screen Printing Process." *Microelectronics International*, **6** (1) 8–17 (1989)
- Glinski, GP, Bailey, C, Pericleous, KA, "A Non-Newtonian Computational Fluid Dynamics Study of the Stencil Printing Process." *Proc. Inst. Mech. Eng. C*, **215** (4) 437–446 (2001)
- Clements, DJ, Desmulliez, MPY, Abraham, E, "The Evolution of Paste Pressure During Stencil Printing." *Solder Surf. Mt. Tech.*, **19** (3) 9–14 (2007)
- Kapur, N, Abbott, SJ, Dolden, ED, Gaskell, PH, "Predicting the Behavior of Screen Printing." *IEEE Trans. Compon. Packag. Manuf. Technol.*, **3** (3) 508–515 (2010)
- DuPont Conglomerate Company, "DuPont SOLAMET PV 19A Photovoltaic Metallization, Preliminary Technical Data Sheet."
- Yüce, C, Willenbacher, N, "Challenges in Rheological Characterization of Highly Concentrated Suspensions—A Case Study for Screen-printing Silver Pastes." *JoVE*, **122** e55377–e55377 (2017)
- Rudez, R, Pavlic, J, Bernik, S, "Preparation and Influence of Highly Concentrated Screen-Printing Inks on the Development and Characteristics of Thick-Film Varistors." *J. Eur. Ceram. Soc.*, **35** (11) 3013–3023 (2015)
- Debeda-Hickel, H, Lucat, C, Menil, F, "Influence of the Densification Parameters on Screen-Printed Component Properties." *J. Eur. Ceram. Soc.*, **25** (12) 2115–2119 (2005)
- Lucat, C, Martin, MP, Debeda-Hickel, H, Largeteau, A, Menil, F, "Screen-Printed Varistors: New Strategy for High Non-linear Coefficient." *J. Eur. Ceram. Soc.*, **27** (13–15) 3883–3886 (2007)
- Zargar, RA, Chackrabarti, S, Joseph, S, Khan, MS, Husain, R, Hafiz, AK, "Synthesis and Characterization of Screen Printed ZnO Films for Solar Cell Applications." *Optik*, **126** (23) 4171–4174 (2015)

30. Sarkar, K, Braden, EV, Bonke, SA, Bach, U, Muller-Buschbaum, P, "Screen-Printing of ZnO Nanostructures from Sol-Gel Solutions for Their Application in Dye-Sensitized Solar Cells." *ChemSuschem*, **8** (16) 2696–2704 (2015)
31. Somalu, MR, Yufit, V, Shapiro, IP, Xiao, P, Brandon, NP, "The Impact of Ink Rheology on the Properties of Screen-Printed Solid Oxide Fuel Cell Anodes." *Int. J. Hydrogen Energy*, **38** (16) 6789–6801 (2013)
32. Somalu, MR, Brandon, NP, "Rheological Studies of Nickel/Scandia-Stabilized-Zirconia Screen Printing Inks for Solid Oxide Fuel Cell Anode Fabrication." *J. Am. Ceram. Soc.*, **95** (4) 1220–1228 (2012)
33. Darsono, N, Yonathan, P, Yoon, DH, Kim, J, Kim, Y, "Dispersion and Field Emission Properties of Multi-walled Carbon Nanotubes by High-Energy Milling." *Mater. Chem. Phys.*, **110** (2–3) 363–369 (2008)
34. Yi, HL, Lai, LJ, Jiang, JS, Hua, CC, "Ethylcellulose Colloids Incubated in Dilute Solution." *J. Phys. Chem. B*, **121** (3) 638–648 (2017)
35. Umerova, S, Dulina, I, Ragulya, A, Konstantinova, T, Glazunova, V, "Rheology of Plasticized Screen Printing Pastes Based on Batio<sub>3</sub> Nanopowder." *Appl. Rheol.*, **26** (3) 38–46 (2016)
36. Inukai, K, Takahashi, Y, Murakami, S, Ri, K, Shin, W, "Molecular Weight Dependence of Ethyl Cellulose Adsorption Behavior on (La, Sr)(Ti, Fe) O<sub>3- $\delta$</sub>  Particles in Organic Solvent Pastes and Their Printing Properties." *Ceram. Int.*, **40** (8) 12319–12325 (2014)
37. Inukai, K, Takahashi, Y, Ri, K, Shin, W, "Rheological Analysis of Ceramic Pastes with Ethyl Cellulose for Screen-Printing." *Ceram. Int.*, **41** (4) 5959–5966 (2015)
38. Qin, J, Bai, S, Zhang, W, Liu, Z, Wang, H, "Effects of Organic Medium on Rheological Properties of Silver Pastes for Crystalline Silicon Solar Cells." *Circuit World*, **42** (2) 77–83 (2016)
39. Qin, J, Zhang, W, Liu, Z, Bai, S, "Effects of Polymer Binder on Rheological Properties of Silver Pastes for Screen Printing Front Electrode Films of Solar Cells." *Int. J. Mod. Phys. B*, **29** (10n11) 1540027 (2015)
40. Elementis Specialties, Inc, *Rheology Handbook: A Practical Guide to Rheological Additives*. (2008)
41. Mezger, TG, *The Rheology Handbook: For Users of Rotational and Oscillatory Rheometers*. Vincentz Network GmbH & Co KG, Hanover (2006)
42. Endo, Y, Mitta, R, Watabe, T, Otsuka, H, "Screen Printing Plate for Solar Cell and Method for Printing Solar Cell Electrode." Grant US9216607 B2, 2015
43. Hsu, CP, Guo, RH, Hua, CC, Shih, C-L, Chen, W-T, Chang, T-I, "Effect of Polymer Binders in Screen Printing Technique of Silver Pastes." *J. Polym. Res.*, **20** (10) 277 (2013)
44. Sachsenheimer, D, Hochstein, B, Willenbacher, N, "Experimental Study on the Capillary Thinning of Entangled Polymer Solutions." *Rheol. Acta*, **53** (9) 725–739 (2014)
45. Martinie, L, Buggisch, H, Willenbacher, N, "Apparent Elongational Yield Stress of Soft Matter." *J. Rheol.*, **57** (2) 627–646 (2013)
46. Larson, RG, *The Structure and Rheology of Complex Fluids*. Oxford University Press, New York (1999)
47. Aoki, M, Nakamura, K, Tachibana, T, Sumita, I, Hayashi, H, Asada, H, Ohshita, Y, "30  $\mu\text{m}$  Fine-Line Printing for Solar Cells." Proc. Photovoltaic Specialists Conference (PVSC), 2013 IEEE 39th, 2013